Bioactive Materials 6 (2021) 4053–4064

Contents lists available at ScienceDirect

Bioactive Materials

journal homepage: www.sciencedirect.com/journal/bioactive-materials

Ca^{2+}-supplying black phosphorus-based scaffolds fabricated with microfluidic technology for osteogenesis

Zhanrong Li [a,1], Xingcai Zhang [d,e,1], Jiang Ouyang [c,1], Dandan Chu [a], Fengqi Han [a], Liuqi Shi [a], Ruixing Liu [a], Zhihua Guo [a], Grace X. Gu [f], Wei Tao [c,*], Lin Jin [a,b,**], Jingguo Li [a,***]

[a] Henan Provincial People's Hospital, Zhengzhou University People's Hospital, Zhengzhou, 450003, People's Republic of China
[b] International Joint Research Laboratory for Biomedical Nanomaterials of Henan, Zhoukou Normal University, Zhoukou, 466001, People's Republic of China
[c] Center for Nanomedicine, Brigham and Women's Hospital, Harvard Medical School, Boston, MA, 02115, United States
[d] School of Engineering and Applied Sciences, Harvard University, Cambridge, MA, 02138, United States
[e] School of Engineering, Massachusetts Institute of Technology, Cambridge, MA, 02139, United States
[f] Department of Mechanical Engineering, University of California, Berkeley, CA, 94720-1740, United States

ARTICLE INFO

Keywords:
Black phosphorus
Bone defect
Osteogenesis
Artificial bone scaffold
Biomineralization

ABSTRACT

Effective osteogenesis remains a challenge in the treatment of bone defects. The emergence of artificial bone scaffolds provides an attractive solution. In this work, a new biomineralization strategy is proposed to facilitate osteogenesis through sustaining supply of nutrients including phosphorus (P), calcium (Ca), and silicon (Si). We developed black phosphorus (BP)-based, three-dimensional nanocomposite fibrous scaffolds via microfluidic technology to provide a wealth of essential ions for bone defect treatment. The fibrous scaffolds were fabricated from 3D poly (L-lactic acid) (PLLA) nanofibers (3D NFs), BP nanosheets, and hydroxyapatite (HA)-porous SiO_2 nanoparticles. The 3D BP@HA NFs possess three advantages: i) stably connected pores allow the easy entrance of bone marrow-derived mesenchymal stem cells (BMSCs) into the interior of the 3D fibrous scaffolds for bone repair and osteogenesis; ii) plentiful nutrients in the NFs strongly improve osteogenic differentiation in the bone repair area; iii) the photothermal effect of fibrous scaffolds promotes the release of elements necessary for bone formation, thus achieving accelerated osteogenesis. Both in vitro and *in vivo* results demonstrated that the 3D BP@HA NFs, with the assistance of NIR laser, exhibited good performance in promoting bone regeneration. Furthermore, microfluidic technology makes it possible to obtain high-quality 3D BP@HA NFs with low costs, rapid processing, high throughput and mass production, greatly improving the prospects for clinical application. This is also the first BP-based bone scaffold platform that can self-supply Ca^{2+}, which may be the blessedness for older patients with bone defects or patients with damaged bones as a result of calcium loss.

1. Introduction

Bone defects, which can be created by traumatic injury, tumor excision, or infectious diseases such as osteitis and osteomyelitis, present a great challenge and burden in clinical surgery [1]. It is estimated that the annual number of patients who suffer from traumatic injury in the US is over 1 million, and many of which may give rise to devastating bone defects, with costs over $10 billion [2]. Furthermore, bone defects with a diameter greater than 3 cm are less likely to heal on their own, leading to a high incidence of complications, pain, and lower quality of life [3,4]. Although therapeutic strategies for bone defects such as autografts and allografts have reached clinical practice, several limitations their therapeutic effect. For autografts, drawbacks include insufficient bone mass, inferior availability, potential donor injury, and low size matching. The potential risks of allografts are contamination or infection, rejection reaction or immune response, and disease cross-transmission [5]. Emerging artificial bone scaffolds, which mimic the natural extracellular matrix (ECM), are ideal alternative bone

Peer review under responsibility of KeAi Communications Co., Ltd.
* Corresponding author.
** Corresponding author. Henan Provincial People's Hospital, Zhengzhou University People's Hospital, Zhengzhou, 450003, People's Republic of China.
*** Corresponding author.
E-mail addresses: wtao@bwh.harvard.edu (W. Tao), jinlin_1982@126.com (L. Jin), lijingguo@zzu.edu.cn (J. Li).
[1] These authors contributed equally to this work.

https://doi.org/10.1016/j.bioactmat.2021.04.014
Received 24 November 2020; Received in revised form 29 March 2021; Accepted 9 April 2021

substitutes, since they are likely to have superior biocompatibility, high biodegradability, and superior interaction with host cells [6]. A variety of techniques such as 3D printing, electrospinning, and microfluidics have been employed to manufacture artificial bone scaffolds [7–10]. Microfluidics enables precise manipulation of fluids in a low-cost, fast-processing, high-throughput, and mass-production manner for creating high-quality products [11–15,57] and has attracted increasing attention for the synthesis of artificial bone scaffolds [16]. The feasibility of the mass-production of high-quality artificial bone scaffolds is extremely important for success in the clinical treatment of bone defects. Thus, the exploitation of an artificial bone scaffold with robust osteoinduction, osteoconduction, and osteointegration based on microfluidic technology is an appealing alternative strategy for clinical bone regeneration.

Black phosphorus (BP), one of the emerging two-dimensional (2D) monoelemental material with a unique folded, layered structure [17–19,21,22,53–56], has drawn widespread attention in biomedicine because of its unique combination of physicochemical properties (*e.g.*, good biocompatibility, excellent biodegradability, and prominent photothermal effects) [17,20,23–27]. Notably, the degradation products of BP in the physiological environment are usually non-toxic phosphate ions [17,25,28], and phosphorus accounts for approximately 1% of total human body weight, mainly as a component of bone in the skeleton [7,29]. Recent research has demonstrated that phosphate can facilitate the mineralization of biomimetic calcium phosphate, thereby improving the adhesion, differentiation, and proliferation of bone cells [30,31]. Moreover, other studies have shown that in the physiological environment, the biodegradation products of BP nanosheets can be converted into calcium phosphate nanoparticles with the ability to promote bone regeneration through in situ biomineralization [31,32]. Although these findings suggest that BP can play a positive role in bone defect treatments, all of these BP-based therapeutic platforms use the body's calcium ions in the physiological environment to achieve biomineralization for bone regeneration [33]. Since a certain Ca/P ratio is vital for the bone regeneration process, the therapeutic effect of these calcium-free phosphorus strategies based on BP will be greatly compromised if applied to older patients with bone defects or patients with damaged bones from calcium loss [30]. Therefore, it is highly desirable to design artificial bone scaffolds based on BP nanosheets bearing adjustable levels of nutrients, rich with mineralized ions.

Hydroxyapatite (HA) is the main inorganic component of human and animal bones. It has excellent biocompatibility and bioactivity and can be chemically bonded with other tissues at their interfaces [34,35]. Furthermore, it has a high solubility in the body and can release nontoxic ions that enter the metabolism for the stimulation or induction of bone hyperplasia, thereby promoting the repair of defective tissues [36,37]. Numerous studies have demonstrated that HA not only has osteoinduction capacity, but can also serve as a calcium source for bone regeneration, preventing calcium loss [34,37,38]. Therefore, the complementary combination of HA and BP will ensure an appropriate Ca/P ratio for constructing the desired artificial, multifunctional bone scaffolds for bone regeneration. Silicon (Si) is also an essential trace element associated with bone metabolism and connective tissue growth [39]. Si ions play important roles in activating osteogenic differentiation of mesenchymal stem cells (MSCs), including facilitating bone matrix mineralization, deposition, and recruitment of MSCs [39]. However, most inorganics containing Si are coated with external matrix composites, limiting the release of the Si ions and affecting the direct interaction between Si and surrounding cells [40,41]. Furthermore, these Si-based composites cannot accurately reproduce the inherent hierarchical porous architectures and surface topographies of natural bone that are essential for maintaining cell-material biophysical interactions [39,42,43]. Coating the surface of an artificial bone scaffold with a layer of mesoporous silicon is one alternative strategy to address the above considerations.

Herein we utilized microfluidic technology and fibrous biomaterials to construct three-dimensional (3D) BP@HA nanocomposite fibrous scaffolds (3D BP@HA NFs) for bone regeneration. The 3D BP@HA NFs are made up of HA-porous SiO_2 nanoparticles created via a biomineralization process, BP nanosheets, and poly (L-lactic acid) (PLLA). In this fibrous scaffold, highly biocompatible BP nanosheets have an excellent photothermal effect, achieving controlled ion release for HA-SiO_2 nanoparticles, while P is an important element for bone formation in biomineralization. The HA part of nanoparticles can provide mineral ions for cellular osteogenesis and new bone formation. The prepared porous SiO_2 nanoparticles not only serve as a Si ion depot but can also be an excellent storage medium for HA minerals due to the large number of pores on their surface. In addition, our nanofibrous scaffolds have variable pore size distribution and highly porous interconnected structures, providing a superior microenvironment for cell differentiation and proliferation. Although the use of BP-based materials for bone regeneration has been reported in several recent studies, this is the first report of Ca^{2+}-supplying BP-based scaffolds, which show great promise in the treatment of older patients with bone defects or patients with damaged bones as a result of calcium loss. Moreover, the use of microfluidic technology also paves the way for the mass-production of our high-quality 3D BP@HA NFs. Therefore, fabrication of doped fibrous scaffold with BP nanosheets and HA-SiO_2 nanoparticles through microfluidic technology has great clinical potential for effective 3D cell culture and stem cell osteogenic differentiation, achieving optimal bone regeneration.

2. Materials and methods

2.1. Materials

BP crystals were obtained from Jiangsu Nanfeng Co. (Nanjing, China). PLLA (MW = 135 kDa) polymers were bought from Daigang Polymer (Jinan, China). Dichloromethane (DCM) and dimethylformamide (DMF) were purchased from Guangzhou Chemical Co. and used without further purification.

2.2. Fabrication of the 3D BP@HA NFs

First, porous SiO_2 nanoparticles were prepared using a facile hydrothermal method. In detail, 3.72 g of cetyltrimethylammonium bromide (CTAB) and trioctylmethylammonium bromide (TOMAB, 2.28 g) were dissolved in 60 °C deionized (DI) water (80 mL) with 300 rpm magnetic stirring for 3 h. Afterward, 360 μL triethylamine (TEA) and tetraethylorthosilane (TEOS, 15% 1-octadecene solution, 40 mL) were continuously added and maintaining at 60 °C for another 3 h under the stirring. Then, the mixture was centrifugated to obtain the silica nanospheres and further washed with water repeatedly to discard residual reactants. The prepared products were dried for 24 h at 100 °C. The final products were further calcined for 10 h at 600 °C to discard the surfactant.

HA was then coated onto SiO_2 nanoparticles through a biomineralization process using 1.5 simulated body fluid solution (1.5 SBF) for 14 days. Briefly, SiO_2 nanoparticles were placed in a 50 mL centrifuge tube, 30 mL 1.5 SBF solution was added into the above centrifuge tube and incubated at 37.0 °C, the fluid was changed every two days. After 14 days of incubation, the HA-coated SiO_2 nanoparticles were washed with deionized water and then dried in a freeze drier. Subsequently, 40 mg of BP crystals were dispersed in the mixed solution (4 mL) of DCM and DMF (DCM: DMF = 1:4, v: v). Then the obtained dispersion was further sonicated in an ice bath with a power of 300 W for 2 h. Next, PLLA (8%, w: v) and HA-coated SiO_2 nanoparticles were added into the above-mixed solution and stirred for 12 h. Finally, 3D BP@HA NFs were fabricated by microfluidic technology as follows: air flow was applied to the solution with suitable pressure, the jet was solidified in air and collected using ethanol, washed by DI water 3–5 times, and freeze-dried.

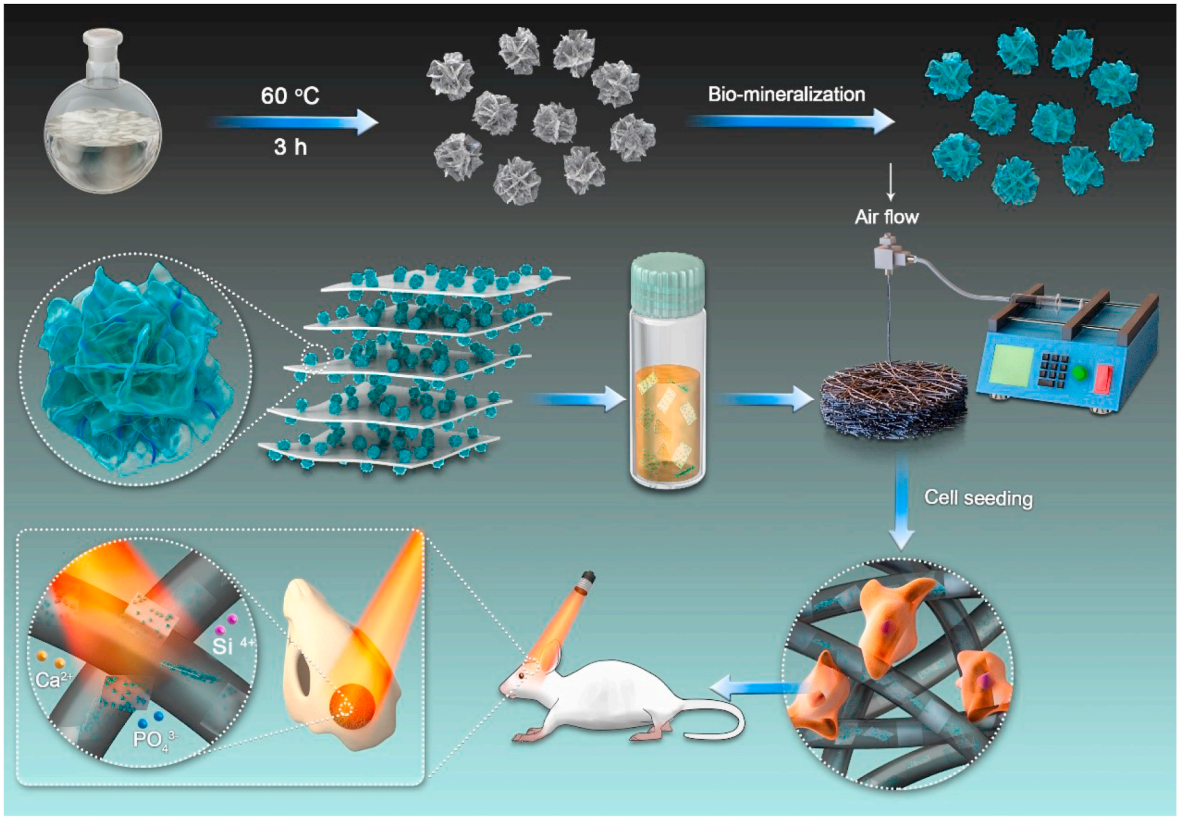

Fig. 1. Fabrication and application of 3D BP@HA NFs, which includes two steps, first preparation of HA-SiO_2, second fabrication 3D BP@HA NFs by microfluidic technology.

2.3. Characterization of 3D BP@HA NFs

The morphology of nanofibers in 3D BP@HA NFs was evaluated using transmission electron microscopy (TEM) and SEM imaging (Quanta 200 scanning electron microscope FEI, Netherlands). The chemical components of 3D BP@HA NFs were characterized using mapping and X-ray diffraction (XRD).

2.4. Cell culture and characterization

BMSCs as model cells were obtained from 2-week-old rats as our described previously [44], and used to assess the cellular interaction between nanofibers of 3D BP@HA NFs and cells. 3D NFs were prepared using a method similar to that used for 3D BP@HA NFs and set as control groups. For cell culture, the 3D BP@HA NFs and 3D NFs were placed into tissue culture plates (24 well, TCP), and sterilized with 75% mixed solution of DI water and ethanol (30min), and treated using ultraviolet light for 4 h. Then the nanofibrous scaffolds were washed 5 times in PBS to remove ethanol, and the cells were cultured into the 3D BP@HA NFs and 3D fluffy PLLA nanofibers at a density of 2.0×10^4 cells/well. 0.5 mL of Dulbecco's Modified Eagle Medium (DMEM) containing 10% FBS (v/v) was then added to each well. These cell-nanofibrous constructs were further cultured under the required environments. During the incubation, the cell medium was changed every two days.

After incubation of 5 days in the 3D BP@HA NFs, the BMSCs were visualized to perform the cellular viability analysis. Firstly, using paraformaldehyde (4.0%) to fix cells for 30 min. Then, 5 μg/mL of Hoechst 33258 (Sigma-Aldrich) and 5 μg/mL of Phalloidin-FITC (Sigma-Aldrich) were employed to perform the staining of cell cytoskeletons and nuclei. Afterward, using a laser scanning confocal microscopy to characterize the cells.

The cellular morphology on the nanofiber surface of 3D BP@HA NFs or 3D NFs was evaluated via SEM imaging. After incubation for 5 days, using glutaraldehyde aqueous solution (3.0%) to fix the cell-BP composite fiber constructs. Afterward, the dehydration was performed via ethanol/water (v/v). The prepared samples were further freeze-dried for 24 h, then imaging was executed after the samples were coated in platinum/palladium with a thickness of 10 nm.

To investigate the cytotoxicity and the cell proliferation of 3D BP@HA NFs, cell counting kit-8 (CCK-8, Dojindo) was utilized at 1, 3, and 7 days. In brief, the BMSCs-seeded fibrous scaffolds were cultured in the CCK-8 solution (10%) for 1 h at 37 °C with 5% CO_2. Then, collecting the supernatant was collected and transferred to the other 96-well plate, and using a microplate reader to test the absorbance at 450 nm of supernatant.

To assess the effect of 3D BP@HA NFs on the osteogenic differentiation of BMSCs, an ALP assay kit (Jiancheng, China) was employed to measure the activity of alkaline phosphatase (ALP) on the 14th day. Firstly, removing the cell medium from each well. Then, rinsing these cells-scaffold composite constructs with PBS, and lysing them via Triton X-100 solution (1%) at room temperature for 30 min. Collecting the lysates and moving to the other 96-well plate for measurement.

To evaluate the mineralization, the Alizarin red staining was performed by quantifying the generation of calcium phosphate (Cyagen, China). After incubation for 21 days, using paraformaldehyde (4%) to fix the cell-scaffold constructs for 1 h, and then washing the samples 4 times with PBS solution. After that, using Alizarin red solution to stain these constructs for 15 min.

2.5. Bone regeneration in vivo

To investigate the bone formation *in vivo*, we established a rat cranial bone defect model. Female Sprague Dawley rats (SD rats, 8 weeks, 220–250 g) were employed to manufacture the cranial bone defect

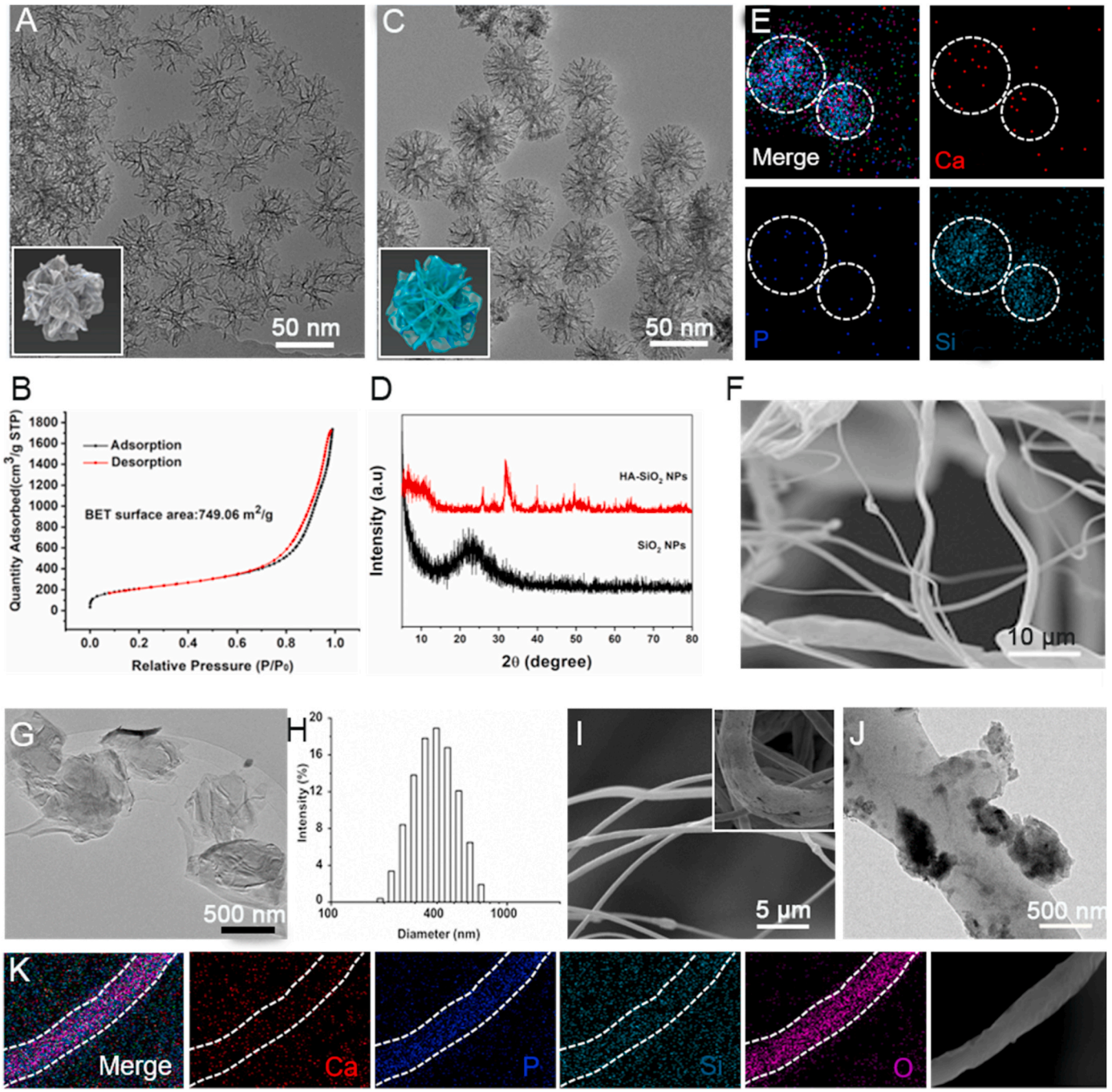

Fig. 2. (A) TEM images of SiO_2 nanoparticles. (B) Nitrogen adsorption-desorption isotherm of SiO_2 nanoparticles. (C) TEM images of HA-SiO_2 nanoparticles. (D) XRD pattern of HA-SiO_2 nanoparticles. (E) Elemental mapping of HA-SiO_2 nanoparticles. (F) SEM images of PLLA NFs fabricated by microfluidic technology. (G) TEM image of BP nanosheets. (H) The size distribution of prepared BP nanosheets. (I) SEM images of porous 3D BP@HA NFs (insert: an enlarged high-definition picture of nanofibers). (J) TEM image of 3D BP@HA NFs. (K) Elemental mapping of nanofiber in 3D BP@HA NFs.

model. In detail, 10% chloral hydrate (0.4 mL/100 g) was used to anesthetize all rats through intraperitoneal injection. Then, the scalps of rats were shaved and disinfected using betadine. In the incisal suture area, a midline dermo-periosteal incision was created, and the defects with a diameter of 6-mm in the skull bones were made through a trephine after the exposure of the cranium under the periosteum. Subsequently, 3D scaffolds (sterile) seeded with BMSCs were incubated into the site of bone defects, and using surgical sutures to suture the incision. Then, using betadine to disinfect the wounds. During the photothermal process, the 808 nm laser (1 W/cm^2) was irradiated 3 times per day for 10 min each time. At the 6 and 15 weeks after surgery, the rats were euthanized, and collecting the tissue samples. The obtained samples were fixed with paraformaldehyde (4%).

To investigate the osteogenesis of bone defects after cells-BP@HA NFs transplantation, the fixed samples were decalcified for 2 weeks in EDTA solution and then dehydrating in ethanol and embedding in paraffin. The prepared samples were cut into sections (5 μm of thickness) for the use of hematoxylin and eosin (H&E) staining. In addition, endothelial cell adhesion alizarin red, Masson's staining, and molecule-31 (CD31) were performed to stain the above-mentioned sections. The histomorphological analysis was carried out to quantify the healing response from the H&Estained samples. The new bone was quantified by

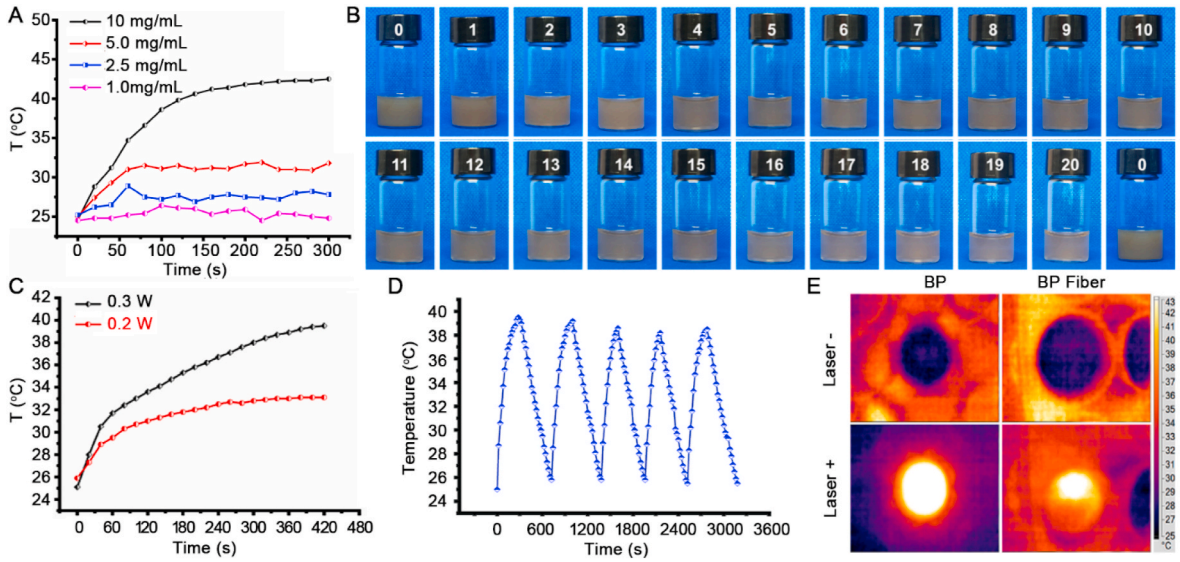

Fig. 3. (A) Photothermal conversion of BP nanosheet aqueous solutions with various concentrations. (B) Photo images of BP nanosheets after 20 repeated NIR exposures. (C) The temperature of 3D BP@HA NFs under NIR exposure. (D) Temperature changes of 3D BP@HA NFs during 5 on/off cycles. (E) Thermal images of 3D BP@HA NFs in the DI water after 5 min NIR exposure.

measuring the area of bone nucleation sites (BNS) in each group using image J software. Alizarin Red staining was quantified. The high-density areas of red staining were identified by using NIS-Elements BR 3.06 (Nikon, Tokyo, Japan) with a quantified total area fraction of calcified nodules. CD31 positive cells were counted in per high power field (HPF) [45].

3. Results and discussion

3.1. Preparation and characterization of 3D BP@HA NFs

As displayed in Fig. 1, the preparation of 3D BP@HA NFs involves the following two steps. First, we prepared HA-SiO_2 nanoparticles using a hydrothermal method and a biomineralization process. Second, the 3D BP@HA NFs were fabricated by a microfluidic technology using PLLA solution (containing prepared HA-SiO_2 nanoparticles and BP nanosheets) as the basic material. The prepared porous SiO_2 nanoparticles with a large number of roughly star-shaped pores have a uniform size distribution of ~80 nm (Figs. 2A and S1A), and a large surface area of 749.06 m^2/g (Fig. 2B). From the transmission electron microscopy (TEM) images, the HA layers were observed after the biomineralization process (Figs. 2C and S1B), and the XRD pattern (Fig. 2D) showed the obvious characteristic peaks of HA (*i.e.*, 211, 112, and 300) after biomineralization [35,46,47]. Moreover, the Ca element appeared in the element mapping of the final nanoparticles (Fig. 2E), indicating the successful binding of HA. Taken all together, these results demonstrated the successful synthesis of HA-SiO_2 nanoparticles [48,49].

It is worth mentioning that, before we moved on to prepare the final 3D BP@HA NFs, pure PLLA NFs were first prepared using either microfluidic technology or electrospinning method. The surface morphology of the PLLA NFs was evaluated by scanning electron microscope (SEM) imaging. We found that the PLLA NFs fabricated by microfluidic technology (Fig. 2F) were not obviously different from that of nanofibers prepared by the electrospinning process (Fig. S2A), and their size distributions were uniform at an average of 800 nm. However, the surface of the PLLA NFs fabricated by microfluidic technology was much smoother than that produced by the electrospinning process. Moreover, the prepared NFs via microfluidic technology had more "fluffy" structures, with the distance between two adjacent 3D NFs around 10 μm and a large number of pores in the scaffold, with the pore size of nanofibers being 10–35 μm. Therefore, besides the mentioned mass-production advantages, microfluidic technology-enabled fluffy 3D NFs may possess more promising advantages in our designed platform.

After confirming this, we then used the microfluidic method to fabricate the designed 3D BP@HA NFs. For their excellent photothermal qualities, BP nanosheets were added to nanofibers. Fig. 2G shows a TEM image of BP nanosheets synthesized by the liquid-phase exfoliation method. As shown, these nanosheets have an average size of 400 nm (200 nm–800 nm), consistent with the size distribution using DLS measure (Fig. 2H). Afterward, the HA-SiO_2 nanoparticles and BP nanosheets mixture were doped with the PLLA solution during the fabrication process to prepare 3D BP@HA NFs. The nanofibers in 3D BP@HA NFs exhibited obvious porous structures (Fig. 2I). The distance between two neighboring nanofibers (i.e., the pore size) ranged from 10 to 30 μm, much larger than that of nanofibrous mats (Fig. S2B), facilitating the easy entry of cells into the interior of the 3D BP@HA NFs scaffold without any external help. Further, the nanofiber diameter of 3D BP@HA NFs ranged from 600 to 900 nm, with an average of 800 nm, and their surface displayed a convex-concave interface structure. The TEM image shows the morphology of HA-SiO_2 nanoparticles on the nanofibers (Fig. S2C), and HA-SiO_2 nanoparticles can be visualized together with the nanofiber. In addition, element mapping (Fig. 2J and K) showed HA-related elements in the nanofibers, such as P and Ca [50]. The EDS pattern (Figs. S2D and S2E) of composite nanofibers displayed rich P content, which majorly originated from BP crystals [51]. These results indicate that BP nanosheets were successfully embedded into the nanofiber with HA-SiO_2 nanoparticles. The final structure of 3D BP@HA NFs establishes the foundation for enabling the 3D cell culture and promoting stem cell osteogenic differentiation.

3.2. Photothermal conversion of 3D BP@HA NFs

Fig. 3A shows the photothermal effect of the BP nanosheets under NIR irradiation with various BP concentrations. Upon 0.3 W/cm^2 NIR laser irradiation, the temperature-increasing trend of BP nanosheets showed obvious dependence on concentration and time, *i.e.*, as both increase, the temperature of the BP nanosheets solution also increased gradually. Notably, the temperature of the 10 mg/mL BP solution rose sharply, reaching 41.4 °C within 180 s, indicating the excellent photothermal performance of BP-based nanosheets. Furthermore, the degradation of BP nanosheets was evaluated through 808 nm laser exposure over 20 repetitions. Fig. 3B showed that after 20 repeated NIR

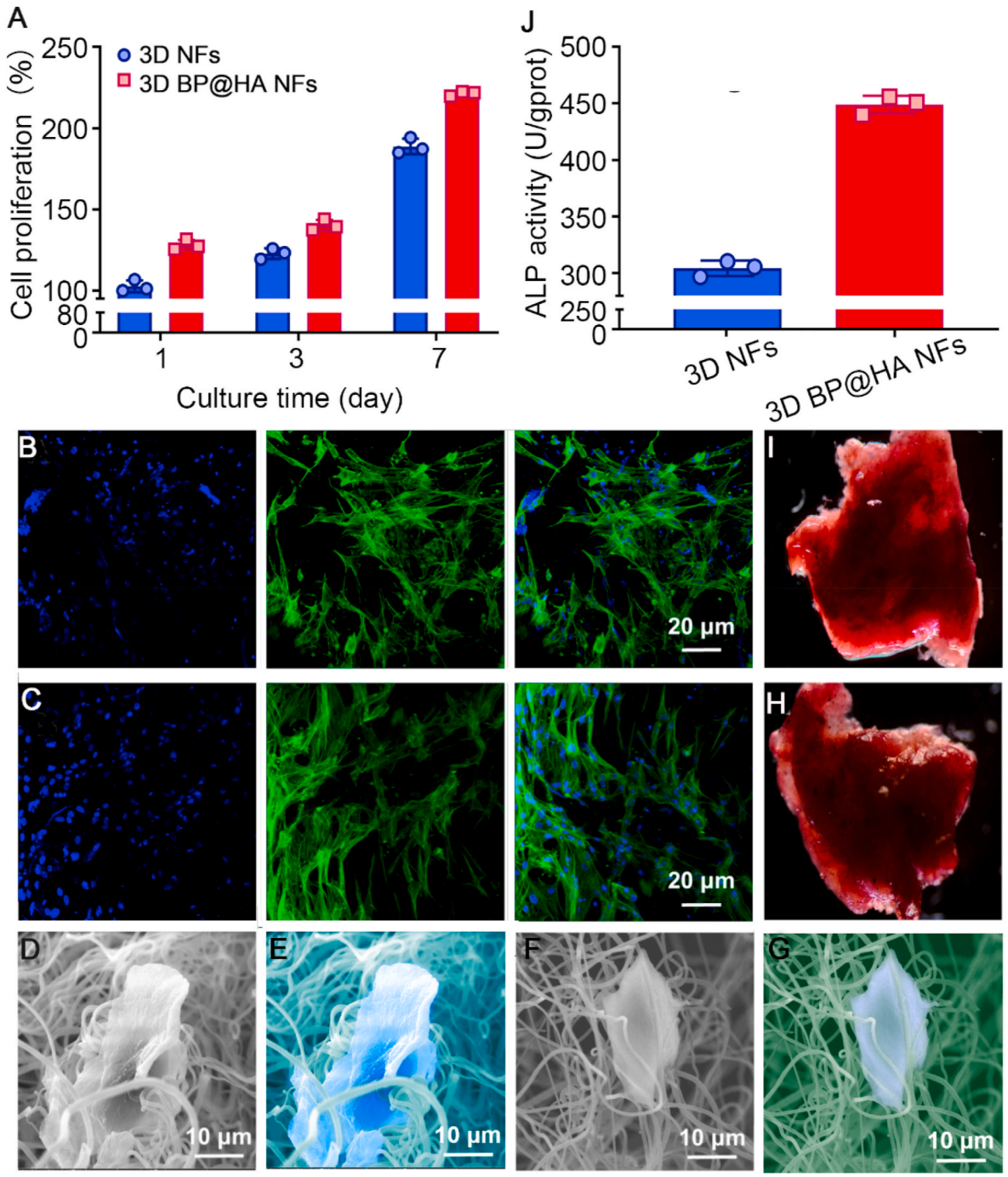

Fig. 4. (A) The proliferation of cells cultured in different samples. (B) Fluorescent images of cells cultured 5 days onto 3D NFs. (C) Fluorescent images of cells cultured 5 days onto 3D BP@HA NFs. (D) SEM images of cells cultured 5 days onto 3D BP@HA NFs and (E) the corresponding pseudo-color SEM. (F) SEM images of cells cultured 5 days onto 3D NFs nanofibers and (G) the corresponding pseudo-color SEM. (H) Alizarin red S staining of BMSCs cultured on 3D BP@HA NFs and (I) 3D NFs. (J) ALP activity of cells cultured for 2 weeks.

exposures, the color of the BP nanosheet solution gradually became paler, and few BP nanosheets remained. This is consistent with a change in BP nanosheet size in which the average hydrodynamic size becomes unstable after NIR exposure, suggesting the disassembly of BP nanosheets (Fig. S3).

BP nanosheets with photothermal effect also endow the 3D BP@HA NFs with good photothermal performance. We next evaluated the photothermal performance of 3D BP@HA NFs. Under the irradiation of a 0.3 W NIR laser, the temperature of 3D BP@HA NFs rapidly increased to 39.5 °C in less than 7 min, much higher compared to the effects of the 0.2 W NIR laser (Fig. 3C). To evaluate the consistency of heat behavior under NIR exposure, the 3D BP@HA NFs were treated with 5 consecutive on/off cycles of NIR irradiation. When the NIR laser was on, the temperature of the 3D BP@HA NFs quickly increased to 38.5 °C. Afterward, turn off the NIR laser, the temperature would be immediately cooled down to the initial temperature (Fig. 3D). The thermal images of 3D BP@HA NFs before and after NIR exposure showed that the local temperature of the nanofibrous scaffold and the surrounding surface rose from 25 °C to 39.5 °C (Fig. 3E), manifesting robust photothermal performance. The above results indicate that the photothermal behavior of 3D BP@HA NFs can be repetitively and remotely controlled using a NIR laser, which can provide desired photothermal effect for bone

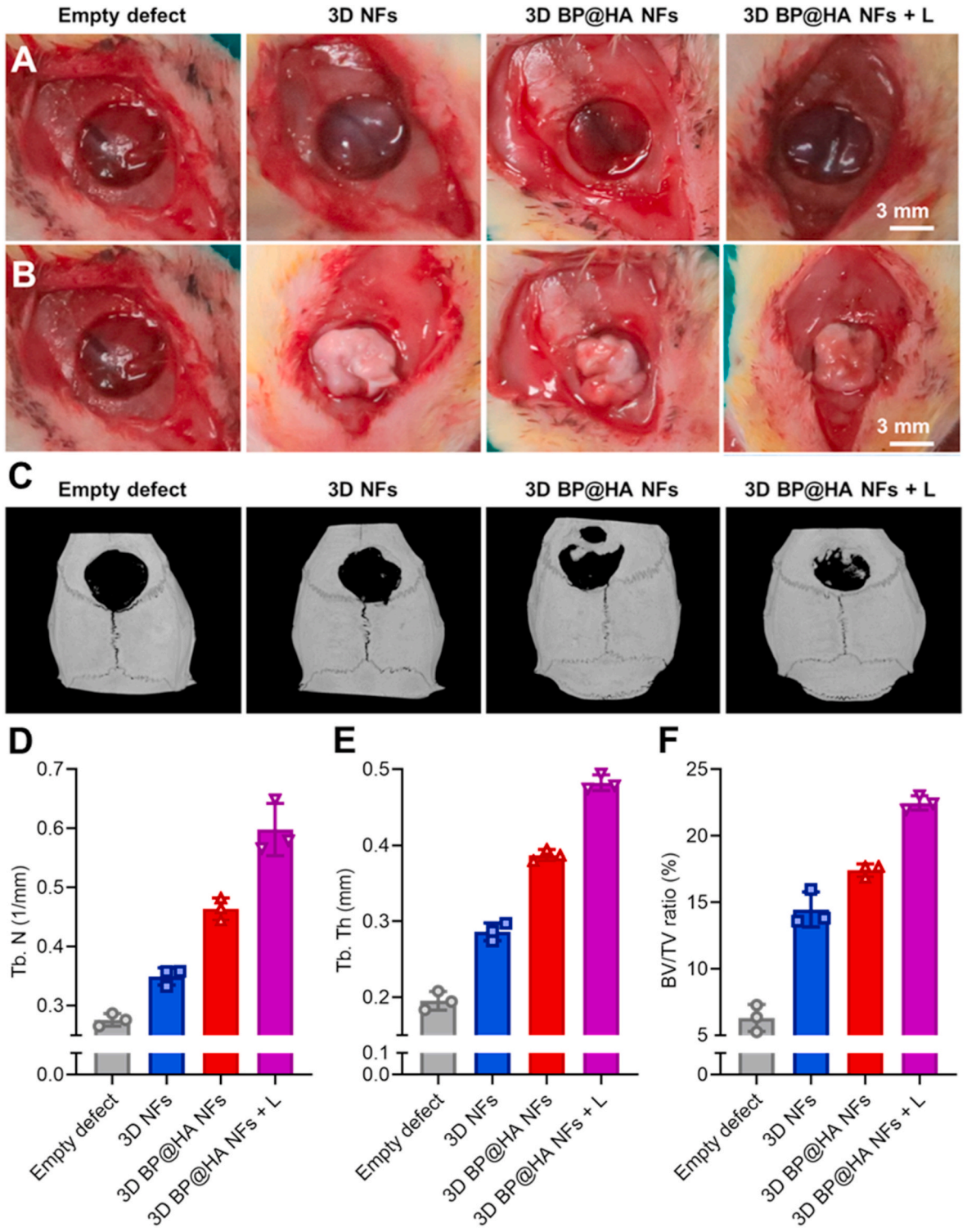

Fig. 5. Photo images of the bone defect models (A) before and (B) after transplantation of BMSCs-scaffold constructs. (C) Micro-CT images of bone defects 15 weeks after BMSCs-scaffold construct implantation. The quantification analysis of related indicators in bone regeneration: (D) Tb. N, (E) Tb. Th, and (F) BV/TV.

regeneration, such as sterilization, drug release, or nutrient release, and blood circulation. In addition, the combination of HA-SiO_2 nanoparticles with BP nanosheets not only endows 3D BP@HA NFs with photo-responsive heating behavior but also provides a large number of osteogenic elements for the new bone formation due to its stable and long-term release. Our 3D BP@HA NFs thus provides an integrated solution for tissue replacement/repair with a localized effect.

3.3. Biocompatibility of 3D BP@HA NFs

To evaluate the effects of the obtained spatial structure of 3D BP@HA NFs on cell incubation, we utilized the CCK-8 assay to evaluate cytotoxicity and cell proliferation. 3D NFs were used as controls. Bone marrow-derived mesenchymal stem cells (BMSCs) were incubated onto the 3D BP@HA NFs and the controls and cultured for 1, 3, and 7 days before the assessment. The results demonstrated that cells on the 3D

BP@HA NFs had a much better attachment than those on the control groups after 1-day incubation (Fig. 4A). After 3 days, the BMSCs in the 3D BP@HA NFs had much higher proliferation than those on the 3D NFs scaffold. At the 7 days, the proliferation of BMSCs in the 3D BP@HA NFs remained higher than that in the 3D NFs scaffold. The above results indicate that the rich elemental nutrients in the "fluffy" spatial structure of the 3D BP@HA NFs may improve cell proliferation. Meanwhile, these positive results also suggested excellent biocompatibility of the nanofibers even after combining the HA-SiO_2.

To evaluate cellular distribution and activity in the nanofibrous scaffold, cellular fluorescence images of the 3D BP@HA NFs (5 days culture) were checked with the confocal microscope. Cells were stained using FITC (fluorescein isothiocyanate) and DAPI (4′,6-diamidino-2-phenylindole). Similar to the cells in 3D NFs (Fig. 4B), most cells in the 3D BP@HA NFs were fully extended (Fig. 4C), exhibiting obvious 3D growth and uniform distribution. The above results indicated that the fluffy spatial nanofibrous structure of 3D BP@HA NFs might enable the cells to easily enter the composite nanofibrous scaffolds and achieved 3D cell culture. There were no significant differences in activity and morphology between 3D BP@HA NFs and 3D NFs. Furthermore, the prepared 3D nanofibrous scaffold provides a superior 3D microenvironment for cell culture and growth.

To investigate the morphology of cells incubated in 3D BP@HA NFs, the cells cultured for 5 days was characterized via SEM. BMSCs in the 3D BP@HA NFs spread widely, and a single integrated cell-fiber construct was obviously formed (Fig. 4D and **E**), which was possibly ascribed to the abundant nutrient elements available, providing a superior microenvironment for cells. Additionally, we observed that the surface of nanofibers in 3D BP@HA NFs was slightly changed, which may be due to the absorption of nanosheets or nanoparticles by BMSCs for differentiation and growth. In comparison, in 3D NFs, the cells grew along fibers, which produced a significant contraction of the nanofibers (Fig. 4F and **G**). Therefore, the nanofibers in the 3D BP@HA NFs provided the required elements for cell growth, proliferation, and differentiation such as Ca, Si, and P, along with the excellent spatial structure for cells to achieve 3D growth.

3.4. Osteogenic differentiation of 3D BP@HA NFs

To investigate the effects of 3D BP@HA NFs on the osteogenic differentiation of BMSCs, the mineralization was analyzed via alizarin red S staining. After incubation for 14 days, BMSCs in 3D BP@HA NFs (Fig. 4H) displayed more positive staining with alizarin red S compared to BMSCs on the 3D NFs scaffold (Fig. 4I). In addition, the osteogenic genes of alkaline phosphatase (ALP) activity were tested to analyze the osteogenic capacity (Fig. 4J), the quantified the expression of ALP using RT-qPCR in cells grown for 14 d. The ALP activity results suggested a prominent difference between the 3D BP@HA NFs and the 3D NFs scaffold. The ALP expression of 3D BP@HA NFs was 450 U/gprot, while the ALP expression of 3D NFs was only 306 U/gprot, demonstrating the greatly superior osteogenic capacity of 3D BP@HA NFs, which was consistent with the staining results. These data suggest that the 3D BP@HA NFs facilitate the osteogenic differentiation of BMSCs and provide the necessary elements (*e. g.*, Ca, Si, and P) for growth and differentiation.

In general, these exciting results demonstrate that the new 3D BP@HA NFs played a vital role in the differentiation and proliferation of BMSCs, showing that the appropriate 3D micro-environment and provision of necessary nutrients regulate the osteogenic capacity of BMSCs effectively. Furthermore, different shapes and sizes of the fluffy scaffold could be tailored to meet the demands of clinical applications. Therefore, our 3D BP@HA NFs show excellent potential for future efforts in bone repair and regeneration.

3.5. In vivo bone formation

In this section, we describe the use of rat cranial bone defect models to assess the bone generation of 3D BP@HA NFs under the NIR laser (808 nm) for 10 min, three times every day, the 3D BP@HA NFs without NIR laser and 3D NFs were used as controls. Bone defect models are shown in Fig. 5A, the diameter and thickness of bone defects were 6 mm and 1 mm, respectively. The BMSCs-scaffold constructs were transferred into the defect section after 2 weeks' culture in both the 3D BP@HA NFs and control groups (Fig. 5B), and then the skin wounds were sutured. After 6 and 15 weeks, bone formation in rats with cranial bone defects was characterized by micro-CT imaging. Six weeks after implantation, the results showed that treatment groups differed significantly. New bone generation was found in the bone defect repaired by 3D BP@HA NFs (Fig. S4A) under NIR exposure. Although there was also new bone generation in the group treated with 3D BP@HA NFs without NIR exposure, it was much less than that under NIR exposure. In contrast, there was less bone formation in 3D NFs and empty defects groups compared to 3D BP@HA NFs regardless of NIR exposure. These findings suggest that HA-SiO_2 nanoparticles elicit the superior formation of new bone, which could be attributed to the photothermal properties of BP nanosheets in nanofibers that can regulate the release of nutrient ions such as Ca and Si. Additionally, the biomineralization between Ca ions and the degradation products of BP nanosheets also facilitated bone regeneration. Quantification analysis of micro-CT through bone volume/tissue volume (BV/TV) was also performed to confirm the therapeutic effect of 3D BP@HA NFs under NIR irradiation. As shown in Fig. S4B, the BV/TV ratio for the 3D BP@HA NFs groups without NIR irradiation was only 6.60%, while the BV/TV reached 11.56% for the groups treated with 3D BP@HA NFs with NIR laser, both of which were much higher than the other control groups. Notably, both the trabecular thickness (Tb.Th) and the trabecular number (Tb.N) in the groups treated with 3D BP@HA NFs and NIR irradiation were also higher than the other three groups.

In addition, alizarin red, Masson, and immunohistochemical staining were used to evaluate bone regeneration. After 6 weeks' treatment, results of hematoxylin and eosin (HE) staining (Fig. S5) indicated the absence of calcium nodules from the empty defect section, while the 3D NFs scaffold displayed a few calcium nodules, demonstrating that the scaffold-cells constructs had a positive effect. For BP@HA NFs without NIR exposure, a little calcium, which was nearly the same as the 3D NFs was seen. For BP@HA NFs under NIR exposure, sections displayed far more calcium than those without NIR exposure. These results indicate that BP@HA NFs under NIR exposure provide many more osteogenic elements for new bone formation than without NIR exposure, and compared to 3D NFs. In addition, consistent with the previous studies, the osteogenic ability of BMSCs was well improved after periodic and appropriate NIR irradiation due to the expression of HSPs, which played an important role in promoting osteogenesis. For example, HSP 47 and HSP 70 are two kinds of typical HSPs in mammalian cells, which could promote osteogenesis. HSP 70 is closely related to the thermo-resistance of cells. Especially, HSP 47 is specific to heat shock, which is indispensable for the biosynthesis and molecular maturation of osteogenesis-related type I collagen by modulating the cross-linking of collagen to generate a unique ECM. The 3D BP@HA NFs could up-regulate the expressions of cellular HSPs, thereby promoting osteogenesis by remotely controlled NIR irradiation [52]. Furthermore, compared with the other three groups, Masson staining images of 3D BP@HA NFs under NIR exposure demonstrated the best curative effect in bone regeneration. Moreover, Masson staining (Fig. S6), alizarin red staining (Fig. S7), and CD31 (Fig. S5) images of 3D BP@HA NFs displayed similar trends. Over time, bone formation changed after 15 weeks' implantation. From the micro-CT images (Fig. 5C), we found that the bone formation in all groups had increased compared to that at 6 weeks. Meanwhile, the osteogenesis of the 3D BP@HA NFs groups under NIR exposure was much better than that without NIR treatment. Additionally, 3D BP@HA

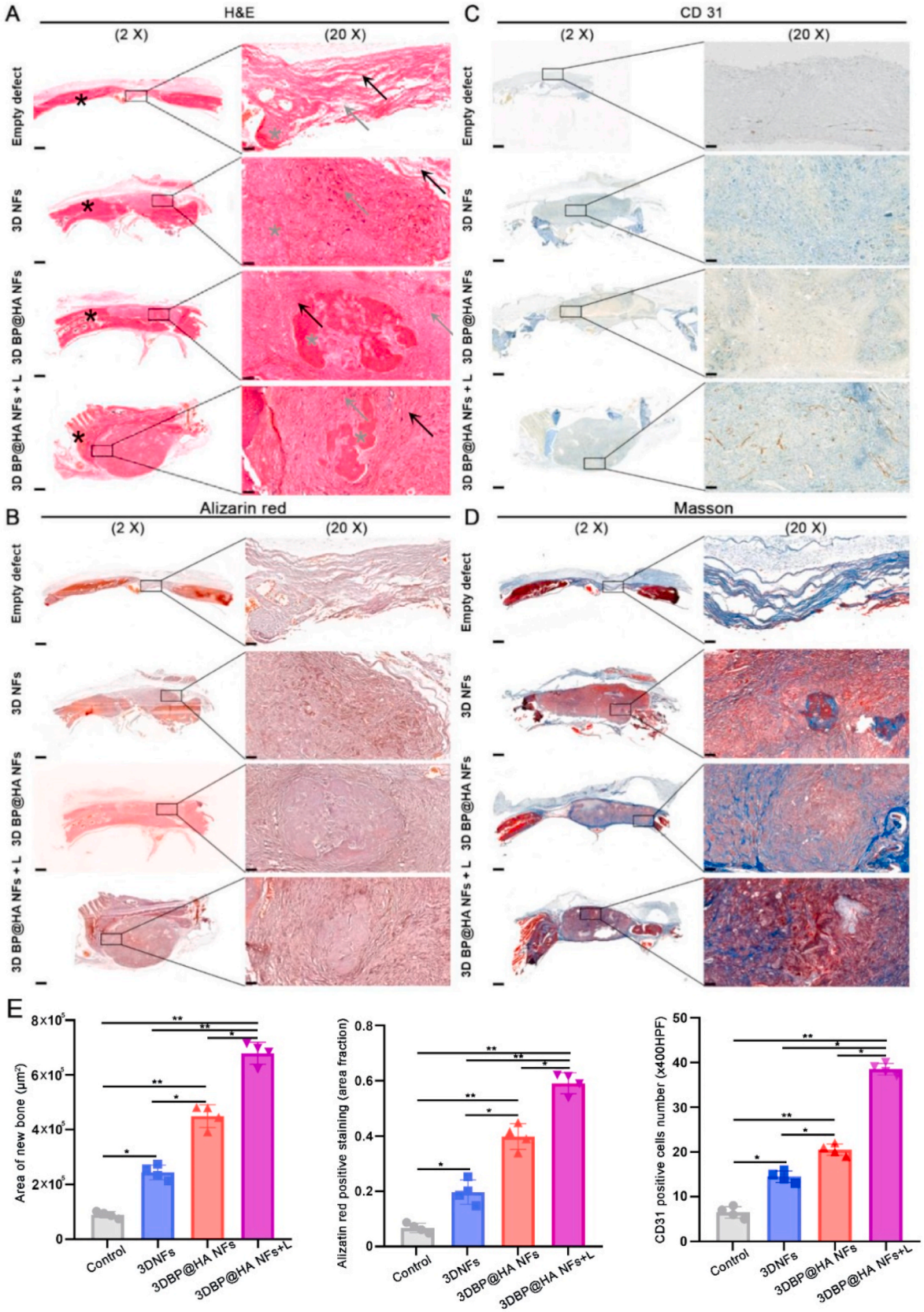

Fig. 6. (A) H&E, (B) Alizarin red, (C) CD31, and (D) Masson staining images of defects in various scaffolds after 15 weeks' BMSCs-scaffold construct implantation. (E) Area of new bone, histomorphological analysis and quantification of alizarin red and CD31 positive staining revealed significant differences among groups. (*$p < 0.05$, **$p < 0.001$). Data plotted represents mean ± standard deviation ($n = 4$). Scale bar : 500 μm for 2 X, 50 μm for 20 X.

NFs groups also displayed much better bone regeneration than either the 3D NFs or empty defects groups. Importantly, the BV/TV of 3D BP@HA NFs groups (Fig. 5F) with NIR treatment was much higher than the groups without NIR: 21.96% and 17.68%, respectively. After 15 weeks of treatment, a similar trend in Tb.N (Fig. 5D) and Tb.Th (Fig. 5E) was found compared with 6 weeks' treatment.

Importantly, after 15 weeks of treatment for the groups of the 3D BP@HA NFs with NIR irradiation, the bone formation grew denser with the fibrous tissue after the *in vivo* implantation. From the H&E images (Fig. 6A), after NIR irradiation, a large number of cell infiltration was observed in the 3D BP@HA NFs, which was much more than the groups without NIR exposure and the groups of 3D NFs scaffold. From the alizarin red staining images (Fig. 6B, E), for the 3D BP@HA NFs under NIR exposure, we could find that newly formed bone trabeculae was surrounded by spindle-shaped cells in the lacunae area. Furthermore, osteocyte-like cells were observed in the bony islands, and capillaries including red blood cells (RBCs) can be found around the area of bone trabeculae. However, the effect was not as obvious in the groups treated with 3D BP@HA NFs without NIR exposure as in the groups with NIR exposure. In contrast, for the control groups and empty defect groups, fewer capillaries and bony islands were observed in the 3D NFs. These results also confirmed that the number of capillaries in the 3D BP@HA NFs was much larger than that in 3D NFs, showing a similar trend to the above in vitro experimental results. In addition, in the 3D BP@HA NFs, samples with NIR exposure displayed visible brown staining areas in bone trabeculae-like structures, as well as the positive staining of CD31 (Fig. 6C, E). Masson staining (Fig. 6D) also indicated the significant formation of cartilage collagen. In comparison, there were only a few calcium nodules (brown) scattered in the 3D BP@HA NFs without NIR exposure and 3D NFs control groups, along with a lower CD31 expression, accord with the H&E and alizarin red staining results. Furthermore, Fig. 6E also confirmed that the laser-activated scaffold significantly enhanced and accelerated new bone formation compared to other groups after 15 weeks.

4. Conclusions

Here, we provided the first proof-of-concept use of Ca^{2+}-supplying black phosphorus-based scaffolds, which were assembled from BP nanosheets, nanofibers, and HA-porous SiO_2 nanoparticles through microfluidic technology, for bone regeneration and tissue engineering. The prepared 3D BP@HA NFs contain adjustable levels of nutritional elements, are rich in mineralized ions, and also have a capacity for on-demand heating for ion release to strengthen osteogenesis. The BP nanosheets in this fibrous scaffold not only endow the 3D BP@HA NFs with excellent photothermal performance but also provide a P source for bone regeneration through biomineralization. Furthermore, the HA-SiO_2 nanoparticles also offer essential nutrients (*e.g.*, Ca and Si) for bone regeneration and greatly facilitate new bone formation. The use of microfluidic technology in the preparation of 3D BP@HA NFs also bodes well for obtaining high-quality nanocomposite fibrous scaffolds at low cost, rapid processing, high throughput, and mass production, all necessary for larger-scale clinical applications. More importantly, the obtained 3D BP@HA NFs create a microenvironment that maintains the stability of the connected pores within the scaffold, which allows BMSCs to easily enter the interior of 3D fibrous scaffolds, achieving bone repair and osteogenesis. We believe that our newly developed 3D BP@HA NFs have excellent potential in bone tissue engineering.

CRediT authorship contribution statement

Zhanrong Li: Conceptualization, Methodology, Writing – original draft. **Xingcai Zhang:** Writing – original draft, Writing – review & editing. **Jiang Ouyang:** Writing – review & editing. **Dandan Chu:** Conceptualization, Methodology, Writing – original draft. **Fengqi Han:** Methodology. **Liuqi Shi:** Methodology. **Ruixing Liu:** Investigation. **Zhihua Guo:** Methodology. **Grace X. Gu:** Validation. **Wei Tao:** Writing – review & editing, Supervision. **Lin Jin:** Resources, Methodology, Writing – review & editing. **Jingguo Li:** Resources, Writing – review & editing, Validation, Supervision.

Declaration of competing interest

The authors declare that they have no known competing financial interests or personal relationships that could have appeared to influence the work reported in this paper.

Acknowledgments

This work was supported by the National Natural Science Foundation of China (U1904176, 81600775, and 21504082; to J.L.), Zhongyuan Thousand Talents Plan Project (to J.L.), Harvard Medical School/Brigham and Women's Hospital Department of Anesthesiology-Basic Scientist Grant (2420 BPA075, to W.T.), Center for Nanomedicine Research Fund (2019A014810, to W.T.), and Gillian Reny Stepping Strong Center for Trauma Innovation Breakthrough Innovator Award (113548, to W. T.).

Appendix A. Supplementary data

Supplementary data to this article can be found online at https://doi.org/10.1016/j.bioactmat.2021.04.014.

References

[1] X. Wang, J. Jin, R. Hou, M. Zhou, X. Mou, K. Xu, Y. Zhu, Z. Shen, X. Zhang, Differentiation of bMSCs on Biocompatible, biodegradable, and biomimetic scaffolds for largely defected tissue repair, ACS Appl. Bio Mater. 3 (2019) 735, https://doi.org/10.1021/acsabm.9b01063.

[2] Y. Qing, R. Li, S. Li, Y. Li, X. Wang, Advanced black phosphorus nanomaterials for bone regeneration, Int. J. Nanomed. 15 (2020) 2045–2058, https://doi.org/10.2147/ijn.s246336.

[3] S. Luo, S. Wu, J. Xu, X. Zhang, L. Zou, R. Yao, L. Jin, Y. Li, Osteogenic differentiation of BMSCs on MoS_2 composite nanofibers with different cell seeding densities, Appl. Nanosci. 10 (2020) 3703–3716, https://doi.org/10.1007/s13204-020-01473-0.

[4] S. Rigal, P. Merloz, D. Le Nen, H. Mathevon, A.-C. Masquelet, Bone transport techniques in posttraumatic bone defects, Orthop. Traumatol. Surg. Res. 98 (2012) 103–108, https://doi.org/10.1016/j.otsr.2011.11.002.

[5] Z. Li, D. Chu, G. Chen, L. Shi, L. Jin, X. Zhang, G. Li, Biocompatible and biodegradable 3D double-network fibrous scaffold for excellent cell growth, J. Biomed. Nanotechnol. 15 (2019) 2209–2215, https://doi.org/10.1166/jbn.2019.2846.

[6] Y. Wang, X. Hu, L. Zhang, C. Zhu, J. Wang, Y. Li, Y. Wang, C. Wang, Y. Zhang, Q. Yuan, Bioinspired extracellular vesicles embedded with black phosphorus for molecular recognition-guided biomineralization, Nat. Commun. 10 (2019) 2829, https://doi.org/10.1038/s41467-019-10761-5.

[7] B. Yang, J. Yin, Y. Chen, S. Pan, H. Yao, Y. Gao, J. Shi, 2D-black-phosphorus-reinforced 3D-printed scaffolds: a stepwise countermeasure for osteosarcoma, Adv. Mater. 30 (2018) 1705611, https://doi.org/10.1002/adma.201705611.

[8] L. Jin, X. Guo, D. Gao, G. Tan, N. Du, X. Wang, Y. Zhang, Z. Yang, X. Zhang, NIR-responsive MXene nanobelts for wound healing, NPG Asia Mater. 13 (2021) 24, https://doi.org/10.1038/s41427-021-00289-w.

[9] R. Huang, X. Chen, Y. Dong, X. Zhang, Y. Wei, Z. Yang, W. Li, Y. Guo, J. Liu, Z. Yang, H. Wang, L. Jin, MXene composite nanofibers for cell culture and tissue engineering, ACS Appl. Bio Mater. 3 (2020) 2125–2131, https://doi.org/10.1021/acsabm.0c00007.

[10] Y. Hou, W. Xie, K. Achazi, J.L. Cuellar-Camacho, M.F. Melzig, W. Chen, R. Haag, Injectable degradable PVA microgels prepared by microfluidic technology for controlled osteogenic differentiation of mesenchymal stem cells, Acta Biomater. 77 (2018) 28–37, https://doi.org/10.1016/j.actbio.2018.07.003.

[11] M.S. Chowdhury, W. Zheng, S. Kumari, J. Heyman, X. Zhang, P. Dey, D.A. Weitz, R. Haag, Dendronized fluorosurfactant for highly stable water-in-fluorinated oil emulsions with minimal inter-droplet transfer of small molecules, Nat. Commun. 10 (2019) 4546, https://doi.org/10.1038/s41467-019-12462-5.

[12] S. Han, Q. Zhang, X. Zhang, X. Liu, L. Lu, J. Wei, Y. Li, Y. Wang, G. Zheng, A digital microfluidic diluter-based microalgal motion biosensor for marine pollution monitoring, Biosens. Bioelectron. 143 (2019) 111597, https://doi.org/10.1016/j.bios.2019.111597.

[13] L. Liu, N. Xiang, Z. Ni, X. Huang, J. Zheng, Y. Wang, X. Zhang, Step emulsification: high-throughput production of monodisperse droplets, Biotechniques 68 (2020) 114–116, https://doi.org/10.2144/btn-2019-0134.

[14] Y. Wang, L. Lu, G. Zheng, X. Zhang, Microenvironment-controlled micropatterned microfluidic model (mmmm) for biomimetic in situ studies, ACS Nano 14 (2020) 9861–9872, https://doi.org/10.1021/acsnano.0c02701.
[15] Z. Tang, N. Kong, X. Zhang, Y. Liu, P. Hu, S. Mou, P. Liljeström, J. Shi, W. Tan, J. S. Kim, Y. Cao, R. Langer, K.W. Leong, O.C. Farokhzad, W. Tao, A materials-science perspective on tackling COVID-19, Nat. Rev. Mater. 5 (2020) 847–860, https://doi.org/10.1038/s41578-020-00247-y.
[16] J. Wu, G. Li, T. Ye, G. Lu, R. Li, L. Deng, L. Wang, M. Cai, W. Cui, Stem cell-laden injectable hydrogel microspheres for cancellous bone regeneration, Chem. Eng. J. 393 (2020) 124715, https://doi.org/10.1016/j.cej.2020.124715.
[17] W. Tao, N. Kong, X. Ji, Y. Zhang, A. Sharma, J. Ouyang, B. Qi, J. Wang, N. Xie, C. Kang, H. Zhang, O.C. Farokhzad, J.S. Kim, Emerging two-dimensional monoelemental materials (xenes) for biomedical applications, Chem. Soc. Rev. 48 (2019) 2891–2912, https://doi.org/10.1039/C8CS00823J.
[18] C. Liu, H.S. Kim, M. Won, E. Jung, J.S. Kim, Navigating 2D monoelemental materials (xenes) for cancer nanomedicine, Matter 3 (2020) 12–13, https://doi.org/10.1016/j.matt.2020.06.004.
[19] C. Feng, J. Ouyang, Z. Tang, N. Kong, Y. Liu, L. Fu, X. Ji, T. Xie, O.C. Farokhzad, W. Tao, Germanene-based theranostic materials for surgical adjuvant treatment: inhibiting tumor recurrence and wound infection, Matter 3 (2020) 127–144, https://doi.org/10.1016/j.matt.2020.04.022.
[20] X. Ji, Y. Kang, J. Ouyang, Y. Chen, D. Artzi, X. Zeng, Y. Xiao, C. Feng, B. Qi, N. Y. Kim, P.E. Saw, N. Kong, O.C. Farokhzad, W. Tao, Synthesis of ultrathin biotite nanosheets as an intelligent theranostic platform for combination cancer therapy, Adv. Sci. 6 (2019) 1901211, https://doi.org/10.1002/advs.201901211.
[21] W. Tao, X. Ji, X. Xu, M.A. Islam, Z. Li, S. Chen, P.E. Saw, H. Zhang, Z. Bharwani, Z. Guo, J. Shi, O.C. Farokhzad, Antimonene quantum dots: synthesis and application as near-infrared photothermal agents for effective cancer therapy, Angew Chem. Int. Ed. Engl. 56 (2017) 11896–11900, https://doi.org/10.1002/anie.201703657.
[22] W. Tao, X. Ji, X. Zhu, L. Li, J. Wang, Y. Zhang, P.E. Saw, W. Li, N. Kong, M.A. Islam, T. Gan, X. Zeng, H. Zhang, M. Mahmoudi, G.J. Tearney, O.C. Farokhzad, Two-dimensional antimonene-based photonic nanomedicine for cancer theranostics, Adv. Mater. 30 (2018), e1802061, https://doi.org/10.1002/adma.201802061.
[23] W. Chen, J. Ouyang, H. Liu, M. Chen, K. Zeng, J. Sheng, Z. Liu, Y. Han, L. Wang, J. Li, L. Deng, Y.-N. Liu, S. Guo, Black phosphorus nanosheet-based drug delivery system for synergistic photodynamic/photothermal/chemotherapy of cancer, Adv. Mater. 29 (2017) 1603864, https://doi.org/10.1002/adma.201603864.
[24] W. Tao, X. Zhu, X. Yu, X. Zeng, Q. Xiao, X. Zhang, X. Ji, X. Wang, J. Shi, H. Zhang, L. Mei, Black phosphorus nanosheets as a robust delivery platform for cancer theranostics, Adv. Mater. 29 (2017) 1603276, https://doi.org/10.1002/adma.201603276.
[25] Z. Tang, N. Kong, J. Ouyang, C. Feng, N.Y. Kim, X. Ji, C. Wang, O.C. Farokhzad, H. Zhang, W. Tao, Phosphorus science-oriented design and synthesis of multifunctional nanomaterials for biomedical applications, Matter 2 (2020) 297–322, https://doi.org/10.1016/j.matt.2019.12.007.
[26] N. Kong, X. Ji, J. Wang, X. Sun, G. Chen, T. Fan, W. Liang, H. Zhang, A. Xie, O. C. Farokhzad, W. Tao, Ros-mediated selective killing effect of black phosphorus: mechanistic understanding and its guidance for safe biomedical applications, Nano Lett. 20 (2020) 3943–3955, https://doi.org/10.1021/acs.nanolett.0c01098.
[27] K. Hu, L. Xie, Y. Zhang, M. Hanyu, Z. Yang, K. Nagatsu, H. Suzuki, J. Ouyang, X. Ji, J. Wei, H. Xu, O.C. Farokhzad, S.H. Liang, L. Wang, W. Tao, M.-R. Zhang, Marriage of black phosphorus and Cu2+ as effective photothermal agents for pet-guided combination cancer therapy, Nat. Commun. 11 (2020) 2778, https://doi.org/10.1038/s41467-020-16513-0.
[28] J. Yang, X. Zhang, C. Liu, Z. Wang, L. Deng, C. Feng, W. Tao, X. Xua, W. Cui, Biologically modified nanoparticles as theranostic bionanomaterials, Prog. Mater. Sci. 118 (2021) 100768, https://doi.org/10.1016/j.pmatsci.2020.100768.
[29] J. Ouyang, X. Ji, X. Zhang, C. Feng, Z. Tang, N. Kong, A. Xie, J. Wang, X. Sui, L. Deng, Y. Liu, J.S. Kim, Y. Cao, W. Tao, In situ sprayed NIR-responsive, analgesic black phosphorus-based gel for diabetic ulcer treatment, Proc. Natl. Acad. Sci. U.S. A. 117 (2020) 28667–28677, https://doi.org/10.1073/pnas.2016268117.
[30] K. Huang, J. Wu, Z. Gu, Black phosphorus hydrogel scaffolds enhance bone regeneration via a sustained supply of calcium-free phosphorus, ACS Appl. Mater. Interfaces 11 (2019) 2908–2916, https://doi.org/10.1021/acsami.8b21179.
[31] J. Shao, C. Ruan, H. Xie, P.K. Chu, X.-F. Yu, Photochemical activity of black phosphorus for near-infrared light controlled in situ biomineralization, Adv. Sci. 7 (2020) 2000439, https://doi.org/10.1002/advs.202000439.
[32] Z. Wang, J. Zhao, W. Tang, L. Hu, X. Chen, Y. Su, C. Zou, J. Wang, W.W. Lu, W. Zhen, R. Zhang, D. Yang, S. Peng, Multifunctional nanoengineered hydrogels consisting of black phosphorus nanosheets upregulate bone formation, Small 15 (2019) 1901560, https://doi.org/10.1002/smll.201901560.
[33] W. Pan, C. Dai, Y. Li, Y. Yin, L. Gong, J.O.a. Machuki, Y. Yang, S. Qiu, K. Guo, F. Gao, Prp-chitosan thermoresponsive hydrogel combined with black phosphorus nanosheets as injectable biomaterial for biotherapy and phototherapy treatment of rheumatoid arthritis, Biomaterials 239 (2020) 119851, https://doi.org/10.1016/j.biomaterials.2020.119851.
[34] Z. Li, D. Chu, Y. Gao, L. Jin, X. Zhang, W. Cui, J. Li Biomimicry, biomineralization, and bioregeneration of bone using advanced three-dimensional fibrous hydroxyapatite scaffold, Mater. Today Adv. 3 (2019) 100014, https://doi.org/10.1016/j.mtadv.2019.100014.
[35] M. Milazzo, N. Contessi Negrini, S. Scialla, B. Marelli, S. Farè, S. Danti, M. J. Buehler, Additive manufacturing approaches for hydroxyapatite-reinforced composites, Adv. Funct. Mater. 29 (2019) 1903055, https://doi.org/10.1002/adfm.201903055.
[36] A.K. Teotia, D.B. Raina, C. Singh, N. Sinha, H. Isaksson, M. Tägil, L. Lidgren, A. Kumar, Nano-hydroxyapatite bone substitute functionalized with bone active molecules for enhanced cranial bone regeneration, ACS Appl. Mater. Interfaces 9 (2017) 6816–6828, https://doi.org/10.1021/acsami.6b14782.
[37] X. Li, Y. Yuan, L. Liu, Y.-S. Leung, Y. Chen, Y. Guo, Y. Chai, Y. Chen, 3D printing of hydroxyapatite/tricalcium phosphate scaffold with hierarchical porous structure for bone regeneration, Bio-Design and Manufacturing 3 (2020) 15–29, https://doi.org/10.1007/s42242-019-00056-5.
[38] E. Quinlan, A. López-Noriega, E. Thompson, H.M. Kelly, S.A. Cryan, F.J. O'Brien, Development of collagen-hydroxyapatite scaffolds incorporating plga and alginate microparticles for the controlled delivery of rhbmp-2 for bone tissue engineering, J. Contr. Release 198 (2015) 71–79, https://doi.org/10.1016/j.jconrel.2014.11.021.
[39] S.-J. Wang, D. Jiang, Z.-Z. Zhang, Y.-R. Chen, Z.-D. Yang, J.-Y. Zhang, J. Shi, X. Wang, J.-K. Yu, Biomimetic nanosilica–collagen scaffolds for in situ bone regeneration: toward a cell-free, one-step surgery, Adv. Mater. 31 (2019) 1904341, https://doi.org/10.1002/adma.201904341.
[40] J. Friguglietti, S. Das, P. Le, D. Fraga, M. Quintela, S.A. Gazze, D. McPhail, J. Gu, O. Sabek, A.O. Gaber, L.W. Francis, W. Zagozdzon-Wosik, F.A. Merchant, Novel silicon titanium diboride micropatterned substrates for cellilar patterning, Biomateials 244 (2020) 119927, https://doi.org/10.1016/j.biomaterials.2020.119927.
[41] Y. Liu, N. Huang, Y.F. Yue, C.P. Zheng, N. Deng, J. Liu, Bioactive SiO2@Ru nanoparticles for osteogenic differentiation of mesenchymal stme cells via activation of Akt signaling pathways, J. Mater. Chem. B 4 (2016) 4389–4401, https://doi.org/10.1039/C5TB01898F.
[42] E.L. Fong, B.M. Watson, F.K. Kasper, A.G. Mikos, Building bridges: leveraging interdisciplinary collaborations in the development of biomaterials to meet clinical needs, Adv. Mater. 24 (2012) 4995–5013, https://doi.org/10.1002/adma.201201762.
[43] E. Alarçin, X. Guan, S.S. Kashaf, K. Elbaradie, H. Yang, H.L. Jang, A. Khademhosseini, Recreating composition, structure, functionalities of tissues at nanoscale for regenerative medicine, Regen. Med. 11 (2016) 849–858, https://doi.org/10.2217/rme-2016-0120.
[44] Y. Lin, Z.R. Li, W.R. Su, M.L. Lin, W.X. Zhang, L. Yi, W. Qian, D. Liang, U Arto. Role of mesenchymal stem cells on cornea wound healing induced by acute alkaliburn, PloS One 7 (2012), e30842.
[45] R.M. Raftery, C.I. Mencia, G. Chen, B. Cavanagh, C.M. Curtin, S.A. Cryan, F.J. O Brien, Translating the role of osteogenic-angiogenic coupling in bone formation: highly efficient chitosan-pDNA activated scaffolds can accelerate bone regeneration in critical-sized bone defects, Biomaterials 149 (2017) 116–127. https://doi:10.1016/j.biomaterials.2017.09.036.
[46] K. Zhou, P. Yu, X. Shi, T. Ling, W. Zeng, A. Chen, W. Yang, Z. Zhou, Hierarchically porous hydroxyapatite hybrid scaffold incorporated with reduced graphene oxide for rapid bone ingrowth and repair, ACS Nano 13 (2019) 9595–9606, https://doi.org/10.1021/acsnano.9b04723.
[47] J.M. Sadowska, F. Wei, J. Guo, J. Guillem-Marti, M.-P. Ginebra, Y. Xiao, Effect of nano-structural properties of biomimetic hydroxyapatite on osteoimmunomodulation, Biomaterials 181 (2018) 318–332, https://doi.org/10.1016/j.biomaterials.2018.07.058.
[48] A. Moncion, J.S. Harmon, Y. Li, S. Natla, E.C. Farrell, O.D. Kripfgans, J. P. Stegemann, F.M. Martín-Saavedra, N. Vilaboa, R.T. Franceschi, Spatiotemporally-controlled transgene expression in hydroxyapatite-fibrin composite scaffolds using high intensity focused ultrasound, Biomaterials 194 (2019) 14–24, https://doi.org/10.1016/j.biomaterials.2018.12.011.
[49] X. Wang, H.C. Schröder, W.E. Müller, Amorphous polyphosphate, a smart bioinspired nano-/bio-material for bone and cartilage regeneration: towards a new paradigm in tissue engineering, J. Mater. Chem. B 6 (2018) 2385–2412, https://doi.org/10.1039/C8TB00241J.
[50] M. Selvakumar, P. Srivastava, H.S. Pawar, N.K. Francis, B. Das, G. Sathishkumar, B. Subramanian, S.K. Jaganathan, G. George, S. Anandhan, On-demand guided bone regeneration with microbial protection of ornamented spu scaffold with bismuth-doped single crystalline hydroxyapatite: augmentation and cartilage formation, ACS Appl. Mater. Interfaces 8 (2016) 4086–4100, https://doi.org/10.1021/acsami.5b11723.
[51] L. Jin, Z.-Q. Feng, T. Wang, Z. Ren, S. Ma, J. Wu, D. Sun, A novel fluffy hydroxylapatite fiber scaffold with deep interconnected pores designed for three-dimensional cell culture, J. Mater. Chem. B 2 (2014) 129–136, https://doi.org/10.1039/C3TB21219J.
[52] L.P. Tong, Q. Liao, Y.T. Zhao, H. Huang, A. Gao, W. Zhang, X.Y. Gao, W. Wei, M. Guan, P.K. Chu, H.Y. Wang, Near-infrared light control of bone regeneration with biodegradable photothermal osteoimplant, Biomaterials 193 (2019) 1–11. https://dio.org/10.1016/j.biomaterials.2018.12.008.
[53] C. Liu, J. Shin, S. Son, Y. Choe, N. Farokhzad, Z. Tang, Y. Xiao, N. Kong, T. Xie, J. S. Kim, W. Tao, Pnictogens in medicinal chemistry: evolution from erstwhile drugs to emerging layered photonic nanomedicine, Chem. Soc. Rev. 50 (2021) 2260–2279, https://doi.org/10.1039/D0CS01175D.
[54] X. Ji, L. Ge, C. Liu, Z. Tang, Y. Xiao, W. Chen, Z. Lei, W. Gao, S. Blake, D. De, B. Shi, X. Zeng, N. Kong, X. Zhang, W. Tao, Capturing functional two-dimensional nanosheets from sandwich-structure vermiculite for cancer theranostics, Nat. Commun. 12 (2021) 1124, https://doi.org/10.1038/s41467-021-21436-5.
[55] W. Chen, C. Liu, X. Ji, J. Joseph, Z. Tang, J. Ouyang, Y. Xiao, N. Kong, N. Joshi, O. C. Farokhzad, W. Tao, T. Xie, Stanene-based nanosheets for ß-elemene delivery and

ultrasound-mediated combination cancer therapy, Angew. Chem. Int. Ed. 60 (2021) 7155–7164, https://doi.org/10.1002/anie.202016330.

[56] J. Ouyang, L. Zhang, L. Li, W. Chen, Z. Tang, X. Ji, C. Feng, N. Tao, N. Kong, T. Chen, Y. Liu, W. Tao, Cryogenic exfoliation of 2D stanene nanosheets for cancer theranostics, Nano-Micro Lett. 13 (2021) 90, https://doi.org/10.1007/s40820-021-00619-1.

[57] Wang Si, Shen Ziao, Shen Zhenyu, Dong Yuanjun, Li Yanran, Cao Yuxin, Zhang Yanmei, Guo Shengshi, Shuai Jianwei, Yang Yun, Lin Changjian, Chen Xun, Zhang Xingcai, Huang Qiaoling, Machine-learning micropattern manufacturing, Nano Today 38 (2021), 101152, https://doi.org/10.1016/j.nantod.2021.101152.